IVYSPRING INTERNATIONAL PUBLISHER

Theranostics

2019; 9(22): 6719-6733. doi: 10.7150/thno.34857

Research Paper

CMKLR1-targeting peptide tracers for PET/MR imaging of breast cancer

Sarah Erdmann[1], Lars Niederstadt[1], Eva Jolanthe Koziolek[2,3,4], Juan Daniel Castillo Gómez[2], Sonal Prasad[2,3], Asja Wagener[1], Jan Lennart von Hacht[1], Sandy Reinicke[1], Samantha Exner[1], Sebastian Bandholtz[1], Nicola Beindorff[3], Winfried Brenner[2,3,5], Carsten Grötzinger[1,4,5,6] ✉

1. Department of Hepatology and Gastroenterology, Campus Virchow-Klinikum, Charité – Universitätsmedizin Berlin, Berlin, Germany
2. Department of Nuclear Medicine, Campus Virchow-Klinikum, Charité – Universitätsmedizin Berlin, Berlin, Germany
3. Berlin Experimental Radionuclide Imaging Center (BERIC), Campus Virchow-Klinikum, Charité – Universitätsmedizin Berlin, Berlin
4. German Cancer Research Center (DKFZ) Heidelberg, Germany
5. German Cancer Consortium (DKTK), partner site Berlin, Germany
6. Molecular Cancer Research Center (MKFZ), Campus Virchow-Klinikum, Charité – Universitätsmedizin Berlin, Berlin, Germany

✉ Corresponding author: Dr. Carsten Grötzinger. Charité - Universitätsmedizin Berlin, Campus Virchow-Klinikum, Department of Hepatology and Gastroenterology and Molecular Cancer Research Center (MKFZ). Augustenburger Platz 1, D-13353 Berlin, Germany. Phone: +49 30 450559488; Fax: +49 30 45055997; Email: carsten.groetzinger@charite.de

Received: 2019.03.13; Accepted: 2019.07.21; Published: 2019.09.19

Abstract

Background: Molecular targeting remains to be a promising approach in oncology. Overexpression of G protein-coupled receptors (GPCRs) in human cancer is offering a powerful opportunity for tumor-selective imaging and treatment employing nuclear medicine. We utilized novel chemerin-based peptide conjugates for chemokine-like receptor 1 (CMKLR1) targeting in a breast cancer xenograft model.

Methods: By conjugation with the chelator 1,4,7,10-tetraazacyclododecane-1,4,7,10-tetraacetic acid (DOTA), we obtained a family of five highly specific, high-affinity tracers for hybrid positron emission tomography/magnetic resonance (PET/MR) imaging. A xenograft model with target-positive DU4475 and negative A549 tumors in immunodeficient nude mice enabled CMKLR1-specific imaging *in vivo*. We acquired small animal PET/MR images, assessed biodistribution by *ex vivo* measurements and investigated the tracer specificity by blocking experiments.

Results: Five CMKLR1-targeting peptide tracers demonstrated high biological activity and affinity *in vitro* with EC_{50} and IC_{50} values below 2 nM. Our target-positive (DU4475) and target-negative (A549) xenograft model could be validated by *ex vivo* analysis of CMKLR1 expression and binding. After preliminary PET imaging, the three most promising tracers [^{68}Ga]Ga-DOTA-AHX-CG34, [^{68}Ga]Ga-DOTA-KCap-CG34 and [^{68}Ga]Ga-DOTA-ADX-CG34 with best tumor uptake were further analyzed. Hybrid PET/MR imaging along with concomitant biodistribution studies revealed distinct CMKLR1-specific uptake (5.1% IA/g, 3.3% IA/g and 6.2% IA/g 1 h post-injection) of our targeted tracers in DU4475 tumor tissue. In addition, tumor uptake was blocked by excess of unlabeled peptide (6.4-fold, 5.5-fold and 3.4-fold 1 h post-injection), further confirming CMKLR1 specificity. Out of five tracers, we identified these three tracers with moderate, balanced hydrophilicity to be the most potent in receptor-mediated tumor targeting.

Conclusion: We demonstrated the applicability of ^{68}Ga-labeled peptide tracers by visualizing CMKLR1-positive breast cancer xenografts in PET/MR imaging, paving the way for developing them into theranostics for tumor treatment.

Key words: Tumor targeting, PET tracer, Chemokine-like receptor 1, peptide ligand, breast cancer

Introduction

Molecular targeting remains to be one of the most promising approaches in cancer diagnosis and therapy. Targeted tracers in combination with highly sensitive positron emission tomography (PET) may facilitate early tumor recognition and staging as well as therapeutic stratification and response monitoring. While the most widely used PET tracer [^{18}F]fluoro-deoxyglucose ([^{18}F]FDG) enables tumor

detection by glucose metabolic imaging and hence also visualizes non-neoplastic cells and tissues, tumor-specific targeting is aiming to provide more sensitive and precise imaging results with less non-specific background [1]. Preferred molecular targets are considered to localize at the cell surface or within the extracellular matrix (ECM), as tracers can reach them without crossing the cell membrane [2-4]. With either high overexpression or even exclusive target expression in tumor cells, appropriately targeted tracers may lead to improved tumor-to-background ratios and thus higher diagnostic sensitivity and specificity.

G protein-coupled receptors (GPCRs) have emerged as molecular targets in the field of cancer care [5, 6]. Thus, upregulated receptor expression in cancer cells can be utilized for tracer-based tumor imaging, for pharmacological intervention through GPCR signaling modification and for peptide receptor radionuclide therapy (PRRT). Unlike antibodies, small-sized receptor ligands such as peptides have a number of advantages regarding their *in vivo* circulation, biodistribution, tumor penetration and low immunogenic potential [7-10].

Chemokine-like receptor 1 (CMKLR1), a G protein-coupled receptor, and its ligand chemerin are known to be involved in inflammation, adipogenesis and glucose metabolism [11, 12]. CMKLR1 couples via the Gi/o family of G proteins and in cells expressing CMKLR1, chemerin inhibits production of cyclic AMP and promotes phospholipase C activation, IP3 release, calcium mobilization and activation of PI3K and MAPK pathways [13]. A nonameric peptide from the carboxyterminus of chemerin (chemerin-9) has been demonstrated to have equally high affinity for CMKLR1 and full agonistic activity [14]. Dysregulation of the receptor-ligand system has been linked to several pathologies such as metabolic syndrome and cardiovascular diseases [15, 16]. Apart from a study demonstrating recruitment of immune cells and hence an antitumor response in melanoma, the role of the chemoattractant chemerin and its receptors in cancer is largely unknown [17, 18]. Increased CMKLR1 expression, chemerin-mediated tumor cell migration and invasion in esophageal squamous cell carcinoma (ESCC) were found by Kumar et al. [19]. Likewise, CMKLR1 has been implicated in neuroblastoma proliferation [20], hepatocellular carcinoma metastasis [21] and migration/invasion of gastric cancer [22]. CMKLR1 may therefore be a promising target for molecular imaging and targeted radionuclide therapy in overexpressing tumor entities. This study evaluated the potential of a family of novel CMKLR1 peptide-DOTA tracers for PET/MR imaging in a breast cancer animal model.

Material and Methods

Peptides

All peptides and DOTA-peptide conjugates were obtained from peptides&elephants (Hennigsdorf, Germany). They were analyzed by mass spectrometry to confirm the presence of the correct molecular mass. Peptides and peptide conjugates were used at a purity of greater than 95%. Analysis data for peptides and peptide conjugates have been deposited in an open data repository for public access: https://doi.org/10.5281/zenodo.3334766

Cell culture

For *in vitro* analysis, HEK293a stably transfected with huCMKLR1 and $G_{\alpha 16}$ were used. For the *in vivo* mouse model, the human breast cancer cell line DU4475 with endogenous CMKLR1 expression and the target-negative human lung carcinoma cell line A549 were used. All cell lines were obtained from ATCC/LGC Standards (Wesel, Germany) and were cultured in RPMI1640 medium containing 10% fetal bovine serum (both from Biochrom, Berlin, Germany) and, in case of transfected cells, selection agents G418 (Biochrom, Berlin, Germany) and zeocin (Invitrogen, Carlsbad, USA).

Xenografts

For *in vivo* experiments, at least 8-week-old female athymic NMRI-*Foxn1*^{nu} /*Foxn1*^{nu} mice (Janvier Labs, Saint-Berthevin, France) were used. Animal care followed institutional guidelines and all experiments were approved by local animal research authorities. For the generation of tumor xenografts, 5 x 10^6 cells of both DU4475 and A549 cells were inoculated subcutaneously into the right and left shoulder, respectively (1:1 phosphate-buffered saline [PBS]/Matrigel Basement Membrane Matrix High Concentration, Corning, Corning, USA). Part of the animals received SW13 lung cancer cells as a CMKLR1-negative control tumor. For the analysis of biodistribution, only data of DU4475 and A549 xenograft tumors are used. Tumors were allowed to grow for two to four weeks (tumor volume > 100 mm^3) after cell inoculation.

Immunofluorescence

For immunofluorescent staining of tumor tissue, the frozen xenografts were embedded in Tissue-Tek O.C.T Compound (Sakura Finetek, Torrance, USA), trimmed by cryostat (12-18 µm) and transferred on glass slides (Superfrost, Thermo Fisher Scientific, Waltham, USA). Xenograft sections were fixed with

1:1 methanol/acetone for two minutes and air-dried. After washing with PBS (Biochrom, Berlin, Germany), sections were blocked with 2% milk powder (blotting grade; Bio-Rad Laboratories, Hercules, USA) in PBS for 30 minutes. Sections were incubated with the primary anti-CMKLR1 antibody developed in our lab (#21-86; polyclonal from rabbit, immunogenic peptide sequence: SSWPTHSQMDPVGY; 3 µg/mL diluted in 0.1% BSA in PBS) in a wet chamber over night at 4 °C. After washing, sections were incubated with the secondary antibody goat-anti-rabbit-Cy2 (Jackson ImmunoResearch, West Grove, USA; 7.5 µg/mL diluted in 0.1% BSA in PBS) for one hour. After washing with PBS, nuclei staining with 1 µg/mL 4′,6-diamidino-2-phenylindole (DAPI) (Sigma-Aldrich, St. Louis, USA) in PBS followed. Finally, the cryosections were fixed with 96% ethanol for two minutes, embedded with Immu-Mount (Thermo Fisher Scientific, Waltham, USA) and analyzed with a confocal laser-scanning microscope (LSM510, Carl Zeiss, Jena, Germany).

Determination of $LogD_{7.4}$ values

Compounds (3 µL of a 1 mM solution) were diluted into 300 µL PBS pH 7.4 or octanol and mixed. 300 µL of the other phase was added, followed by vigorous mixing using a vortex shaker for one minute. The two phases were centrifuged (5 min, 10,000 x g). Following separation, 25 µL aliquots were removed for HPLC analysis. $LogD_{7.4}$ was calculated by taking the logarithm of the ratio of the high-performance liquid chromatography (HPLC) peak area of each compound in octanol to the corresponding peak area in buffer. Consequently, $logD_{7.4}$ values were based on analysis of both aqueous and octanol fractions.

Calcium mobilization assay

Optical ViewPlate 96-well microplates (PerkinElmer, Waltham, USA) were coated with poly-D-lysine (10 µg/mL, 50 µL/well) for 30 minutes at 37 °C, washed with PBS and air dried before seeding 40,000 HEK293a huCMKLR1 $G_{\alpha 16}$ cells per well. The next day, cells were starved with serum-free medium for 30 minutes and incubated with loading medium consisting of serum-free medium with 2.5 mM probenicid (Sigma-Aldrich, St. Louis, USA) and 2 µM Fluo-4 AM (Thermo Fisher Scientific, Waltham, USA). After a loading time of 45 minutes, cells were washed with 100 µL C1 buffer (130 mM NaCl, 5 mM KCl, 10 mM 4-(2-hydroxyethyl)-1-piperazinee-thanesulfonic acid [HEPES], 2 mM $CaCl_2$, 10 mM glucose) followed by 20 minutes of incubation in the dark. After another washing and incubation cycle, the cell plate was placed into the CellLux Calcium Imaging System (PerkinElmer, Waltham, USA) and the assay was performed automatically according to the following protocol. After a baseline measurement for 30 seconds, the ligands (prepared in C1 buffer with 0.5% BSA in double concentration and pipetted in a U-bottom plate) were added on top of the cells and the fluorescence intensity was recorded for further 60 seconds. Obtained raw data were analyzed using AssayPro (PerkinElmer, Waltham, USA). After spatial uniformity correction, maximum response values (F) were normalized to baseline values (F_0) of each well using the following equation:

$$\text{response} = \Delta F/F_0 = (F - F_0)/F_0.$$

Iodination of chemerin-9

Radioactive iodination of the nonapeptide chemerin-9 (Tyr-Phe-Pro-Gly-Glu-Phe-Ala-Phe-Ser, representing amino acids 149-157 of full-length chemerin) was performed by the chloramine T method [23]. For labeling, 10 nmol of chemerin-9 in 25 µL iodination buffer (0.5 M sodium phosphate, pH 7.4) were mixed with 1 mCi carrier-free Na[^{125}I] (NEZ033L010MC, PerkinElmer, Waltham, USA) in an HPLC glass vial with microvolume insert. The reaction was started by adding 4 µL chloramine T (1 mg/mL in water). After 20-30 seconds, 4 µL of sodium metabisulfite (2 mg/mL in water) were added to stop the iodination. HPLC purification was performed to separate unlabeled from labeled radioactive peptide on an Agilent ZORBAX 300 Extend-C18 column using a gradient from 20 to 50% acetonitrile (+0.1% TFA) against water (+0.1% TFA) for 20 minutes. First, 1-2 µL of the reaction mixture were analyzed to determine the retention time of the radioactive peptide. This fraction was then collected during the main run, diluted with radioactive binding buffer to prevent radiolysis, aliquoted and stored at -20 °C.

Competitive and saturation binding studies

Competitive binding studies were performed with cell membrane preparations. Therefore, cellular monolayer cultures were washed with pre-warmed PBS and dissociated in ice-cold PBS with 5 mM ethylene glycol-bis(β-aminoethyl ether)-N,N,N′,N′-tetraacetic acid (EGTA) (Carl Roth, Karlsruhe, Germany) with the help of a cell scraper. Tumor tissue was homogenized with a rotor-stator homogenizer (Ultra-Turrax T8, IKA-Werke, Staufen, Germany) in ice-cold PBS with 5 mM EGTA. Both, cell and tissue homogenates were centrifuged for ten minutes (4 °C, 200 x g), and supernatants were discarded. Pellets were resuspended in 5 mL of membrane isolation buffer (5 mM TrisHCl pH 7.6, 5 mM $MgCl_2$, 1 mM EGTA, protease inhibitor cocktail cOmplete [Roche Applied Science, Penzberg, Germany]) with a glass dounce tissue grinder (Wheaton, Millville, USA) and

further homogenized by moving the pestle up and down (approx. 30 times). After centrifugation for 30 minutes (4 °C und 40.000 x g), the process was repeated, before cell and tissue homogenates were resuspended in 1 mL membrane isolation buffer, aliquoted and stored at -80 °C. For competitive binding, 5 µg of isolated membrane in 25 µL binding buffer (50 mM HEPES pH 7.4, 5 mM $MgCl_2$, 1 mM $CaCl_2$, 0.5% bovine serum albumin [BSA], protease inhibitor cocktail cOmplete) were incubated with increasing concentrations of non-radioactive peptide (2-fold concentrated in 50 µL) and 100,000 cpm of [^{125}I]Tyr^{149}-chemerin-9 (^{125}I-chemerin-9) (in 25 µL binding buffer). After one hour of incubation at 37 °C, the mixture was transferred to 96-well filter plates (MultiScreen$_{HTS}$ FB Filter Plate 1.0 µm, Millipore, Billerica, USA), unbound peptide was withdrawn by suction and the plate was washed four times with cold washing buffer (50 mM Tris-HCl pH 7.4, 125 mM NaCl, 0.05% BSA). After drying the filter plate, 40 µL scintillation cocktail (Ultima Gold F, Perkin Elmer, Waltham, USA) per well was added and radioactivity was measured by liquid scintillation counting (MicroBeta^2 Microplate Counter, PerkinElmer, Waltham, USA). For saturation binding, binding buffer was prepared with varying concentrations of labeled peptide from 0 to 5 nM, either with (non-specific binding, NSB) or without 5 µM of additional unlabeled peptide (total binding, TB). Saturation binding was performed to determine the maximum number of binding sites B_{max}. Therefore, non-specific binding was subtracted from total binding to obtain specific binding (SB). By non-linear regression (one site - total and non-specific, one site - specific binding), GraphPad Prism 5.04 was used to determine the B_{max} value of DU4475 cells in cpm which was further used to calculate the number of binding sites in fmol per mg membrane protein.

Radiochemical labeling with gallium-68 (^{68}Ga)

Radiolabeling experiments were performed on a Modular Lab PharmTracer synthesis module (Eckert & Ziegler, Berlin, Germany) which allows fully automated cassette-based labeling of gallium tracers utilizing a pharmaceutical grade ^{68}Ge/^{68}Ga generator (GalliaPharm, 1.85 GBq, good manufacturing practice [GMP]-certified; Eckert & Ziegler GmbH, Berlin, Germany). Cassettes were GMP-certified and sterile. They were used without pre-conditioning of the cartridges. The gallium generator was eluted with aqueous HCl (0.1 M, 7 mL) and the eluate was purified on an ion-exchange cartridge followed by elution using 1 mL of 0.1 M HCl in acetone. The peptide-DOTA conjugate (50 µg from a stock solution 1 mg/mL in 10% dimethyl sulfoxide [DMSO] in water) was mixed with 500 µL 0.1 M HEPES buffer (pH 7) and heated for 500 seconds at 95 °C. After the reaction, the mixture was passed through a C-18 cartridge for purification and the tracer was eluted from the cartridge with ethanol. In order to control the quality of radiolabeling, the radiochemical yield, purity, and specific activity for all five peptide-DOTA conjugates and each individual labeling experiment was determined. Overall, a radiochemical yield of 82.1% ± 6.7%, a radiochemical purity of 98.1 ± 4.6% and a molar activity of 8.6 GBq/µmol ± 2.7 GBq/µmol was achieved (Table S1). Before animal injection, the activity was equilibrated to neutral pH using 1 M sodium hydrogen carbonate. It was further diluted with saline to ≤ 10% ethanol.

Radiochemical labeling with lutetium-177 (^{177}Lu)

Radiolabeling of peptide-DOTA conjugates was carried out manually using ^{177}Lu from ITG Isotope Technologies Garching GmbH (Garching, Germany). A total of 50 µL (stock solution of peptide at 1 µg/µL in 10% DMSO in water) was added to 200 µL of acetate buffer (sodium acetate/acetic acid buffer, 0.4 M, pH 5.0) and 120 µL of gentisic solution prepared by dissolving 50 mg of gentisic acid in 1 mL of acetate buffer. The resulting mixture was then added to 35 µL of ^{177}Lu (1 GBq in aqueous 0.04 M HCl) and the reaction mixture was heated at 96 °C for 30 minutes followed by cooling for 10 minutes at room temperature. The product was then diluted with 5 mL of saline and used directly for animal experiments. Radiochemical purity determined by HPLC was found to be higher than 99% in all cases, radiochemical yield was about 95%, and the product had a molar activity of approximately 10 GBq/µmol.

Non-radioactive labeling with ^{nat}Ga, ^{nat}Lu and ^{nat}Y

Non-radioactive complexes of the peptide-DOTA conjugates with native gallium, lutetium, and yttrium were synthesized by incubation of 3 nmol peptide conjugate dissolved in 30 µL buffer (sodium acetate/acetic acid buffer, 0.5 M, pH 5.4) using 10-fold molar excess of the metal ion. The reaction was carried out for 30 minutes at 95° C and followed by HPLC purification on a C18 column.

PET/MR imaging

Positron emission tomography (PET) / magnetic resonance imaging (MRI) (1 Tesla nanoScan PET/MRI, Mediso, Hungary) was performed at the Berlin Experimental Radionuclide Imaging Center (BERIC), Charité – Universitätsmedizin Berlin. A dedicated mouse whole-body coil was used for

RF-transmission and signal receiving. Mice were anesthetized using 1-2% isoflurane/0.5 L/min oxygen. Body temperature was maintained at 37 °C during the time of imaging by using a heated bed aperture. Anatomic whole-body MRI scans were acquired using a high-resolution T2-weighted 2D fast spin echo sequence (T2 FSE 2D) with the following parameters: TR = 8700 ms; TE = 103 ms; slice thickness/gap = 1.1 mm/ 0.1 mm; matrix = 256 x 256 mm; external averages = 5 and number of excitations = 2. PET scans in list mode were acquired either for 30 minutes one and two hours after intravenous injection or for 90 minutes of dynamic imaging starting directly before injection of 0.15 mL of tracer, corresponding to a ^{68}Ga activity of approximately 20 MBq for static 1 h-images and 2 h-images and 15 MBq for kinetic imaging. To determine the effect of unlabeled ligand on the tumor uptake, 200 nmol CG34 peptide (approximately 50-fold excess) was co-injected. Static PET images were reconstructed from the raw data as one image (1 x 1800 s) and dynamic PET images were reconstructed with the image sequence 9 x 600 s. The uptake value (kBq/cm^3) in the tumor tissue was determined by manual contouring of a volume of interest (VOI) of the PET images using PMOD 3.610 (PMOD Technologies, Zürich, Switzerland).

Biodistribution studies

Tumor-bearing mice were injected with approximately 10 MBq of ^{68}Ga-labeled DOTA-peptide or 1 MBq of ^{177}Lu-labeled DOTA-peptide to the tail vein via a catheter. Mice were sacrificed and dissected one or two hours after injection. Tumor, blood, stomach, pancreas, small intestine, colon, liver, spleen, kidney, heart, lung, muscle and femur samples were weighed and uptake of radioactivity was measured by a gamma counter. To determine the effect of unlabeled ligand on the tumor uptake, 200 nmol CG34 peptide (100-fold excess) was co-injected.

Statistical analysis

All statistical analyses were performed using GraphPad Prism 5.04. EC_{50}/IC_{50} values were determined by nonlinear sigmoidal curve fitting with variable slope setting, and normalized response for competitive binding results. Multiple group comparisons were done by a two-way ANOVA and Bonferroni post hoc test. All presented data are based on independent experiments. Normalizations and statistics are further defined in each figure legend.

Data availability

Numerical data for all experiments (xlsx file) have been deposited in an open data repository for public access: https://doi.org/10.5281/zenodo.3334766

Results

Characterization of an endogenously CMKLR1-expressing tumor mouse model

As model for tracer testing, the human breast cancer cell line DU4475, which endogenously expresses high levels of CMKLR1, and the target-negative human lung cancer cell line A549 were chosen to induce subcutaneous xenograft tumors in nude mice. Analysis of *ex vivo* tumor tissue confirmed CMKLR1 expression in DU4475 xenografts by immunostaining, whereas A549 tumors showed no detectable antigen (Figure 1A). To confirm presence of receptor protein in DU4475 cells with an independent method, saturation binding studies were performed on membrane preparations of cultured cells (Figure 1B). The assessment of total (TB) and non-specific binding (NSB) of ^{125}I-labeled chemerin-9 was used to determine the specific binding (SB) of the radioligand to CMKLR1 and further to calculate the maximum number of binding sites B_{max} (27.40 ± 2.97 fmol/mg). Competitive binding studies were used for comparison of both cell lines *in vitro* and *ex vivo* (Figure 1C). Receptor binding of ^{125}I-labeled chemerin-9 in DU4475 cell membrane preparations (*in vitro*) led to values around 200 cpm (assessment of radioactivity by liquid scintillation counting) which could be significantly blocked (approx. 80 cpm) by an excess of the unlabeled peptide (1 µM). Membranes isolated from DU4475 tumors (*ex vivo*) bound less labeled peptide (approx. 115 cpm) but still exhibited specific binding, as 1 µM chemerin-9 clearly displaced about 50% of the bound activity (60 cpm). In contrast, membrane preparations from A549 cells and xenograft tumors showed no specific binding.

Characterization of high-potency, high-affinity CMKLR1-targeting peptide-DOTA conjugates

Chemical design of five tracers for CMKLR1 targeting involved two peptide analogs (CG34: Y-Cha-Hyp-G-Cit-F-a-Tic-S and CG36: Y-Cha-P-G-M-Y-A-F-f) of the CMKLR1 ligand chemerin-9 (Y-F-P-G-Q-F-A-F-S) that were attached to the chelator 1,4,7,10-tetraazacyclododecane-1,4,7,10-tetraacetic acid (DOTA) via one of four different chemical linkers: 4,7,10-trioxatridecan-succinamic acid (TTDS), 6-aminohexanoic acid (AHX), N-ε-capryloyl-lysine (KCap) and 10-aminodecanoic acid (ADX) (Figure 2A). Due to their chemical composition, both peptide analogs as well as the four linkers exhibit distinct characteristics such as different length and hydrophobicity. In Figure 2A, these conjugate components are depicted in different colors (reddish colors indicate more hydrophobic properties and greenish colors more hydrophilicity). As a

measure for their hydrophobicity, $LogD_{7.4}$ values were determined as -1.01 ± 0.39 for DOTA-TTDS-CG34, -0.96 ± 0.2 for DOTA-AHX-CG34, 1.29 ± 0.68 for DOTA-KCap-CG34, 1.35 ± 0.31 for DOTA-ADX-CG34, and 2.27 ± 0.47 for DOTA-AHX-CG36.

In vitro characterization of the probes was realized by activity and radioligand binding studies in HEK293a cells stably transfected with CMKLR1. Ligand-induced receptor activation as intracellular Ca^{2+} flux was quantified in an intracellular calcium mobilization assay (Figure 2B). Concentration-response profiles for all five tracers were determined and EC_{50} values were calculated. In comparison to the unconjugated peptide analog CG34 (EC_{50} 0.4 nM), the TTDS-linked DOTA conjugate of CG34 had a slightly higher EC_{50} value of 1.51 nM. Receptor affinity was assessed by competitive radioligand binding studies and resulting IC_{50} values were derived (Figure 2C). Furthermore, DOTA conjugates were labeled with non-radioactive gallium (^{nat}Ga) to investigate a potential impact of metal ion complexation on binding affinity. For DOTA-TTDS-CG34, gallium-labeling barely had an effect on receptor binding (IC_{50} value approximately 0.6 nM). As the unconjugated peptide CG34 exhibited an IC_{50} of 1.0 nM, conjugation with DOTA had even increased its binding affinity. Figure 2D summarizes all EC_{50} and IC_{50} values of the five DOTA peptide conjugates. All CG34 conjugates showed EC_{50} values within the low nanomolar range of approx. 0.6 – 1.5 nM, thus, 1.6- to 3.8-fold higher values for receptor activation than for the unconjugated peptide. However, for receptor binding the IC_{50} values were similar to the value for CG34 or even lower (subnanomolar range: approx. 0.3 – 1.0 nM) and non-radioactive gallium labeling did not adversely affect the affinity. Compared to the activating potency (EC_{50} 0.9 nM) and binding affinity (IC_{50} 0.1 nM) of the unconjugated peptide CG36, the DOTA-AHX-CG36 probe exhibited only slightly higher values (EC_{50} 1.53 nM, IC_{50} w/o ^{nat}Ga 0.13 nM and w/ ^{nat}Ga 0.13 nM).

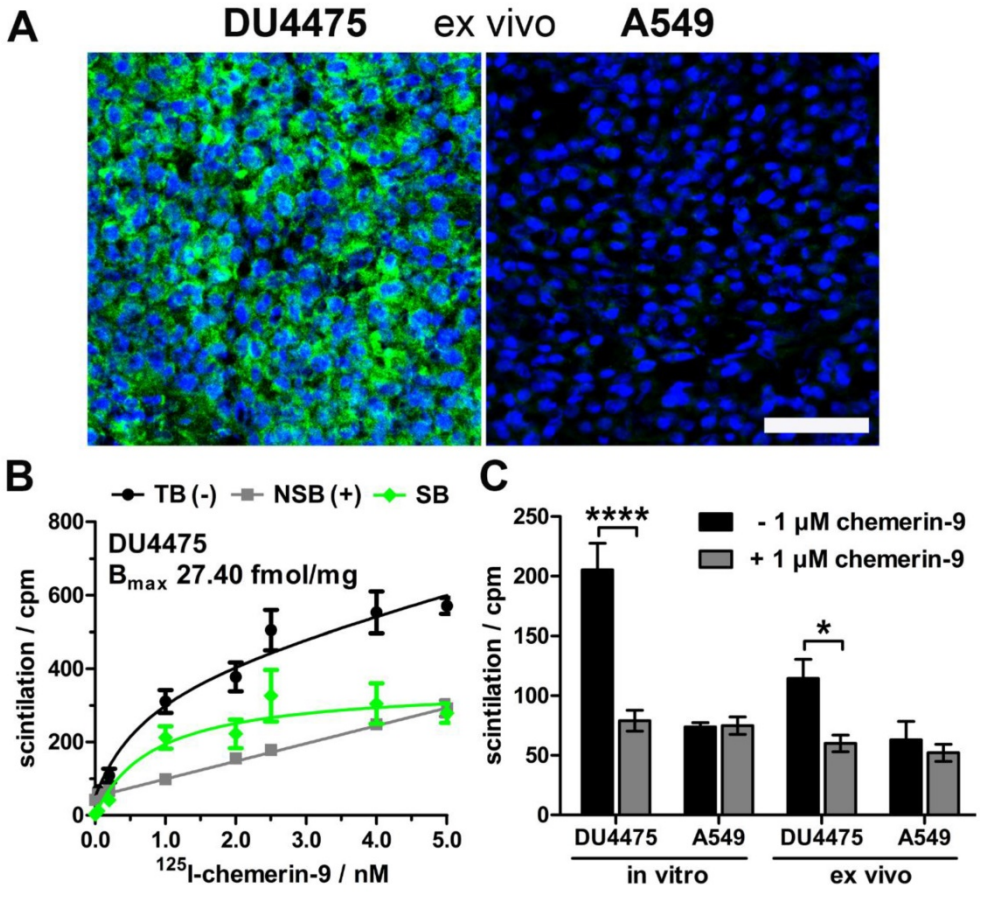

Figure 1: Characterization of the xenograft tumor model. Breast cancer DU4475 and lung cancer A549 cells were employed to establish a xenograft model with both CMKLR1-positive and -negative tumor. **(A)** Immunostaining of xenograft cryosections revealed CMKLR1 immunostaining (green) in DU4475 *ex vivo* tissue whereas the A549 tumor showed no signal. (blue: cell nuclei; bar = 50 µm) **(B)** Saturation binding studies with increasing concentrations of ^{125}I-labeled chemerin-9 allowed analysis of total (TB), non-specific (NSB) and specific binding (SB) to DU4475 cell membranes either without (-) or with (+) blocking excess of 5 µM unlabeled ligand. The B_{max} value for DU4475 cells (27.40 fmol/mg) was then determined by non-linear regression and one site - specific binding analysis. Data were obtained from three independent experiments, values are indicated as means ± SEM. **(C)** Competitive radioligand binding studies using ^{125}I-labeled chemerin-9 showed specific binding to DU4475 cell membranes (*in vitro*) and xenograft tumor membranes (*ex vivo*), which could be blocked by 1 µM unlabeled ligand. In contrast, A549 cells as well as A549 xenografts showed no specific binding. Data were obtained from at least three independent experiments and values are indicated as means ± SEM. (**** $P < 0.0001$, * $P < 0.05$)

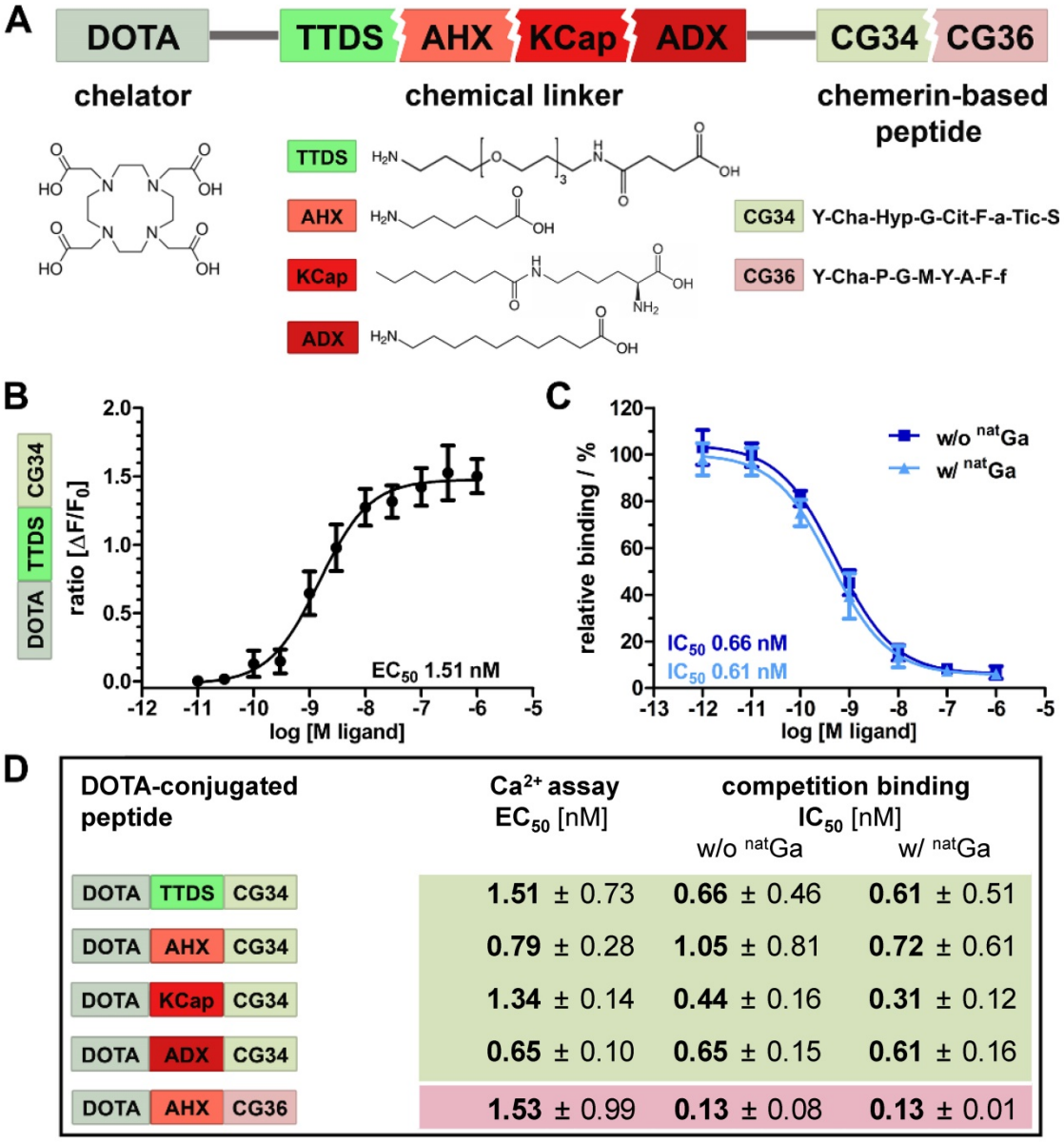

D

DOTA-conjugated peptide	Ca^{2+} assay EC_{50} [nM]	competition binding IC_{50} [nM] w/o ^{nat}Ga	competition binding IC_{50} [nM] w/ ^{nat}Ga
DOTA TTDS CG34	**1.51** ± 0.73	**0.66** ± 0.46	**0.61** ± 0.51
DOTA AHX CG34	**0.79** ± 0.28	**1.05** ± 0.81	**0.72** ± 0.61
DOTA KCap CG34	**1.34** ± 0.14	**0.44** ± 0.16	**0.31** ± 0.12
DOTA ADX CG34	**0.65** ± 0.10	**0.65** ± 0.15	**0.61** ± 0.16
DOTA AHX CG36	**1.53** ± 0.99	**0.13** ± 0.08	**0.13** ± 0.01

Figure 2: Characterization of DOTA peptide conjugates regarding their functionality and affinity. (A) The chelating agent 1,4,7,10-tetraazacyclododecane-1,4,7,10-tetraacetic acid (DOTA) was conjugated to the N-terminus of one of the two optimized chemerin peptide analogs, CG34 and CG36, by one of the four chemical linkers. **(B)** By functional Ca^{2+} mobilization assay, the concentration-response curve for the TTDS-linked CG34 conjugate could be determined and the resulting EC_{50} value (1.51 nM) confirmed its high receptor-activating potency. Response data are presented as mean ± SEM of three independent experiments. **(C)** Ligand affinity to the receptor was assessed by competitive radioligand binding experiments using ^{125}I-chemerin-9 as radioligand. Displacement binding curves revealed similar IC_{50} values of the labeled (with ^{nat}Ga) and unlabeled (without ^{nat}Ga) DOTA conjugate indicating high affinity. Data are shown as mean ± SEM of three independent experiments normalized to non-competed radioligand binding. **(D)** To assess how the conjugation affects the ligand characteristics, functional and affinity data were obtained accordingly for all five chemerin conjugates (summarized as EC_{50}/IC_{50} values). The Ca^{2+} and binding assays were performed with HEK293a cells stably expressing huCMKLR1 and $G_{\alpha 16}$. All EC_{50}/IC_{50} values were obtained from three independent experiments and are indicated as means ± SD. (green colors indicate more hydrophilic, red more hydrophobic properties of peptides and linker)

In vivo PET/MR imaging and biodistribution studies demonstrate specific tracer uptake in CMKLR1-expressing tumors

An initial PET study was performed to estimate the *in vivo* behavior of the five tracer conjugates after ^{68}Ga-labeling. Tumor-bearing mice received an intravenous injection of approximately 20 MBq radiotracer and were imaged for 30 minutes starting one hour post-injection in the PET/MRI scanner. Figure 3 shows *in vivo* PET images of the five tracers, depicted with hydrophobicity increasing from left to right. The most hydrophilic tracer [^{68}Ga]Ga-DOTA-TTDS-CG34 accumulated mainly in the kidneys (Figure 3A, yellow arrow) with no clear DU4475 tumor uptake (right shoulder) compared to the general background. With [^{68}Ga]Ga-DOTA-AHX-CG34, tumor-to-background signal was found to be higher (Figure 3B, white arrow) and accompanied by less kidney uptake. The tracer uptake within the

target-positive tumor on the right shoulder was even more enhanced with KCap as linker (Figure 3C, white arrow). The most hydrophobic CG34 tracer, with ADX as a linker, also led to specific tumor uptake (Figure 3D, white arrow), but also high kidney (yellow arrow) and apparent liver uptake (red arrow). For the tracer [^{68}Ga]Ga-DOTA-AHX-CG36, kidney and liver signals were high but almost no tumor uptake could be detected (Figure 3E). Based on these initial *in vivo* findings, the three most promising tracers [^{68}Ga]Ga-DOTA-AHX-CG34, [^{68}Ga]Ga-DOTA-KCap-CG34 and [^{68}Ga]Ga-DOTA-ADX-CG34 were further analyzed. In addition to PET/MRI scans, *ex vivo* biodistribution studies were performed.

In vivo hybrid imaging with [^{68}Ga]Ga-DOTA-KCap-CG34 and [^{68}Ga]Ga-DOTA-ADX-CG34 using the PET/MRI scanner enabled not only functional PET analysis of the tracers but also allowed to gain anatomical insights into the tumor tissue and volume by high-resolution T2-weighted MR imaging (upper panels, Figure 4). As seen in the T2-weigthed images, both tumors (A549 on the left and DU4475 on the right shoulder) were of comparable size, tissue characteristics and vascularization. The KCap-linked radiotracer apparently accumulated in the DU4475 tumor and in kidneys one hour post-injection with decreasing PET signals after two hours. In contrast, no clear A549 tumor signal could be detected (upper panel, Figure 4A). In addition to *in vivo* imaging, tumor-bearing mice were injected with approximately 10 MBq of radiotracer and sacrificed after one and two hours, respectively. By *ex vivo* measurement, tissue radioactivity was calculated as percentage of injected activity per gram tissue (% IA/g). After one hour, [^{68}Ga]Ga-DOTA-KCap-CG34 led to a DU4475 tumor uptake of about 3.3% IA/g and was 1.4-fold less in the A549 tumor with approx. 2.3% IA/g. Furthermore, higher values were measured for spleen (approx. 4.9% IA/g) and, due to the predominant renal excretion of peptides, for kidneys (approx. 5.8% IA/g). The DU4475 uptake decreased to approx. 2.9% IA/g, whereas the kidney signal increased up to approx. 6.5% IA/g two hours post-injection (lower panel, Figure 4A). For [^{68}Ga]Ga-DOTA-ADX-CG34, the PET signal in DU4475 tumor and kidneys was comparatively stronger one and two hours post-injection than the uptake of [^{68}Ga]Ga-DOTA-KCap-CG34 and there was also an additional distinct liver uptake of the radiotracer (upper panel, Figure 4B). These higher organ uptakes were confirmed by biodistribution data (lower panel, Figure 4B). In addition to overall higher values one hour after injection, liver (approx. 14.2% IA/g), kidney (10.3% IA/g) and spleen (7.8% IA/g) uptakes were the most profound off-target effects. However, with approx. 6.2% IA/g for CMKLR1-positive DU4475 tumors and approx. 2.7% IA/g for target-negative A549 tumors, PET results and tracer specificity could be confirmed. After two hours, DU4475 uptake declined by 1.5-fold to approx. 4.2% IA/g and a distinct liver uptake (approx. 12.5% IA/g) persisted. Kinetic measurements of tracer concentration in tumors, kidneys and liver demonstrated a delayed kidney peak for

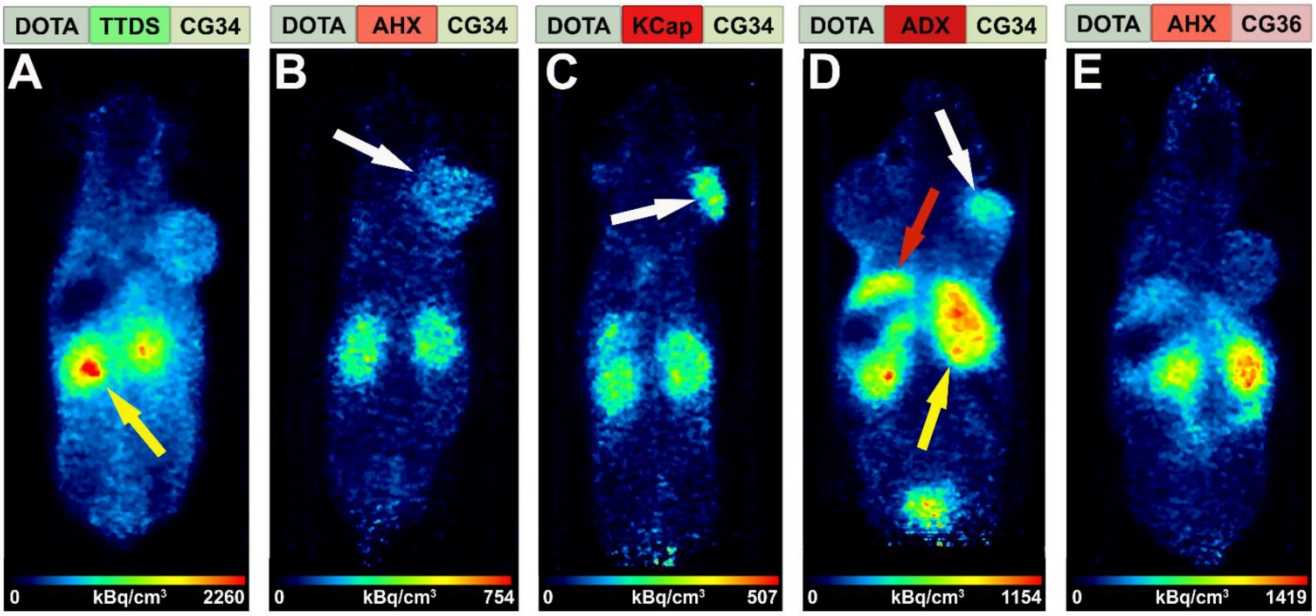

Figure 3: Comparison of tracer biodistribution by PET imaging. Representative static PET images were acquired for 30 minutes one hour post-injection of the five ^{68}Ga-labeled DOTA conjugates in a DU4475/A549 tumor model and revealed a differential distribution. Approximately 20 MBq of each tracer were injected intravenously. **(A)** Predominant renal excretion of the hydrophilic tracer [^{68}Ga]Ga-DOTA-TTDS-CG34 is indicated by a pronounced kidney signal (yellow arrow). **(B-C)** The more hydrophobic linkers AHX and KCap led to less kidney signal, but more distinct DU4475 uptake (white arrows). **(D)** Beside the kidney uptake, [^{68}Ga]Ga-DOTA-ADX-CG34 induced an increased liver signal (red arrow). **(E)** [^{68}Ga]Ga-DOTA-AHX-CG36 showed a comparable kidney and liver uptake, but less accumulation in the DU4475 tumor.

[^{68}Ga]Ga-DOTA-KCap-CG34, with rapid washout from kidneys for both [^{68}Ga]Ga-DOTA-AHX-CG34 and [^{68}Ga]Ga-DOTA-ADX-CG34 (Figure S2). While the other two tracers showed a small decline in the DU4475 tumor, [^{68}Ga]Ga-DOTA-ADX-CG34 appeared to gain in tumor activity until 90 minutes p.i.

Receptor blocking studies verify tracer specificity

For further investigation of CMKLR1 specificity of the radiotracers, blocking experiments were carried out. To examine whether tracer binding to the tissues could be displaced, PET/MR imaging was performed twice with the same animal, once with and once without an excess of unlabeled peptide. In parallel, biodistribution experiments under blocking conditions (excess of unlabeled peptide) were performed to confirm PET results independently in a quantitative manner.

Figure 5 shows representative results of *in vivo* receptor blocking experiments with [^{68}Ga]Ga-DOTA-AHX-CG34. PET/MR imaging without excess of the unconjugated and unlabeled peptide CG34 showed DU4475 tumor and kidney signals one hour post-injection (Figure 5A). However, co-injection of 200 nmol CG34 (50-fold excess) led to a complete loss of tumor uptake and a highly enhanced kidney signal (Figure 5B). The tracer biodistribution one hour after

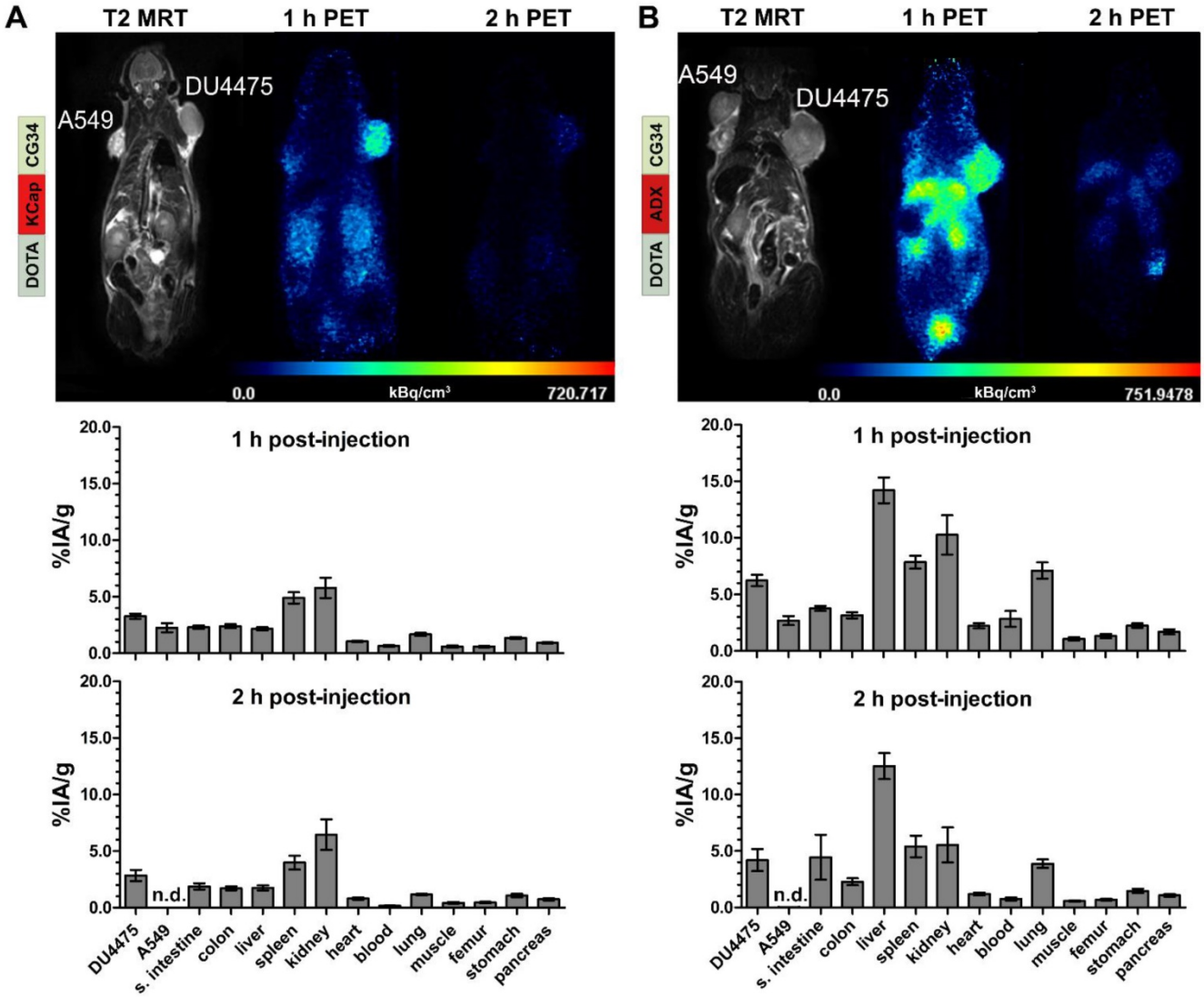

Figure 4: PET/MR imaging and biodistribution study with CMKLR1-targeted, chemerin-based tracers [^{68}Ga]Ga-DOTA-KCap-CG34 and [^{68}Ga]Ga-DOTA-ADX-CG34. Representative static PET images were acquired for 30 minutes one and two hours post-injection (p.i.) of 20 MBq ^{68}Ga-labeled conjugate in DU4475 (target-positive) and A549 (negative) tumor model (upper panel). For quantitative analysis of tracer biodistribution, 10 MBq of the tracer was injected intravenously and tissue was analyzed *ex vivo* one or two hours p.i. Values for tracer uptake are indicated as percent injected activity per gram tissue (% IA/g) (lower panel). **(A)** The T2-weighted MRI image clearly shows both tumors on the animal´s shoulders. The PET images reveal [^{68}Ga]Ga-DOTA-KCap-CG34 uptake in DU4475 after one hour, which decreased two hours p.i. The A549 tumor accumulated much less activity. Beside tumor uptake, the tracer accumulated in the kidneys after one hour. The quantitative analysis of biodistribution one hour p.i indicates more tracer uptake in DU4475 than in A549. Predominant renal excretion is represented by a noticeable kidney value ($3 \leq n \leq 15$; mean ± SEM). **(B)** Injection of [^{68}Ga]Ga-DOTA-ADX-CG34 resulted in strong DU4475 and low A549 uptake. In addition, tracer uptake was detected in kidneys and liver. Quantitative analysis of tracer biodistribution after one hour shows a high uptake in DU4475, and less in A549 tumors. Furthermore, the more hydrophobic tracer accumulated in the kidneys, liver and spleen and led to an overall stronger and longer organ accumulation ($5 \leq n \leq 16$; mean ± SEM). (n.d. = not determined)

injection without competing CG34 clearly demonstrated the distinct DU4475 tumor uptake (approx. 5.1% IA/g) and the high kidney (approx. 6.5% IA/g) and spleen (approx. 6.3% IA/g) values (Figure 5C). CMKLR1 blocking with an excess of CG34 led to an overall low tissue and organ radioactivity except for strong kidney uptake (8.6% IA/g) and excretion into the urinary bladder. The tracer uptake within DU4475 tumors could be blocked by a factor of 6.4 to approximately 0.8% IA/g (Figure 5D).

A summary of all biodistribution data including calculated tissue radioactivity ratios for the three most promising tracers [^{68}Ga]Ga-DOTA-AHX-CG34, [^{68}Ga]Ga-DOTA-KCap-CG34 and [^{68}Ga]Ga-DOTA-ADX-CG34 is presented in Table 1. Use of these CMKLR1 tracers resulted in distinct target-specific DU4475 tumor uptake with 5.1% IA/g ([^{68}Ga]Ga-DOTA-AHX-CG34), 3.3% IA/g ([^{68}Ga]Ga-DOTA-KCap-CG34) and 6.2% IA/g ([^{68}Ga]Ga-DOTA-ADX-CG34). All three of them showed favorable tumor-to-kidneys ratios with 0.9, 0.7 and 0.8. CMKLR1 specificity could be proven by 1.7-fold (5.1 vs. 3.0% IA/g), 1.4-fold (3.3 vs. 2.3% IA/g) and 2.3-fold (6.2 vs. 2.7% IA/g) higher uptake in CMKLR1-positive DU4475 tumors than in target-negative A549 tumors one hour post-injection. In addition, receptor blocking by co-injection of an excess of unlabeled chemerin peptide diminished specific tracer binding by 6.4-fold (5.1 vs. 0.8% IA/g), 5.5-fold (3.3 vs. 0.6% IA/g) and 3.4-fold (6.2 vs. 1.8% IA/g). The most stable and durable tumor uptake was achieved by [^{68}Ga]Ga-DOTA-AHX-CG34 with 4.9% IA/g (approx. 96% of the 1 h-value) after two hours, whereas uptake of the KCap-linked (approx. 88%) and ADX-linked (approx. 68%) tracers declined faster within two hours after injection. The highest overall non-tumor uptake values were seen with [^{68}Ga]Ga-DOTA-ADX-CG34, with considerable liver (14.2% IA/g) and kidney (10.3% IA/g) uptake and hence, the lowest tissue radioactivity ratios for the DU4475 tumor.

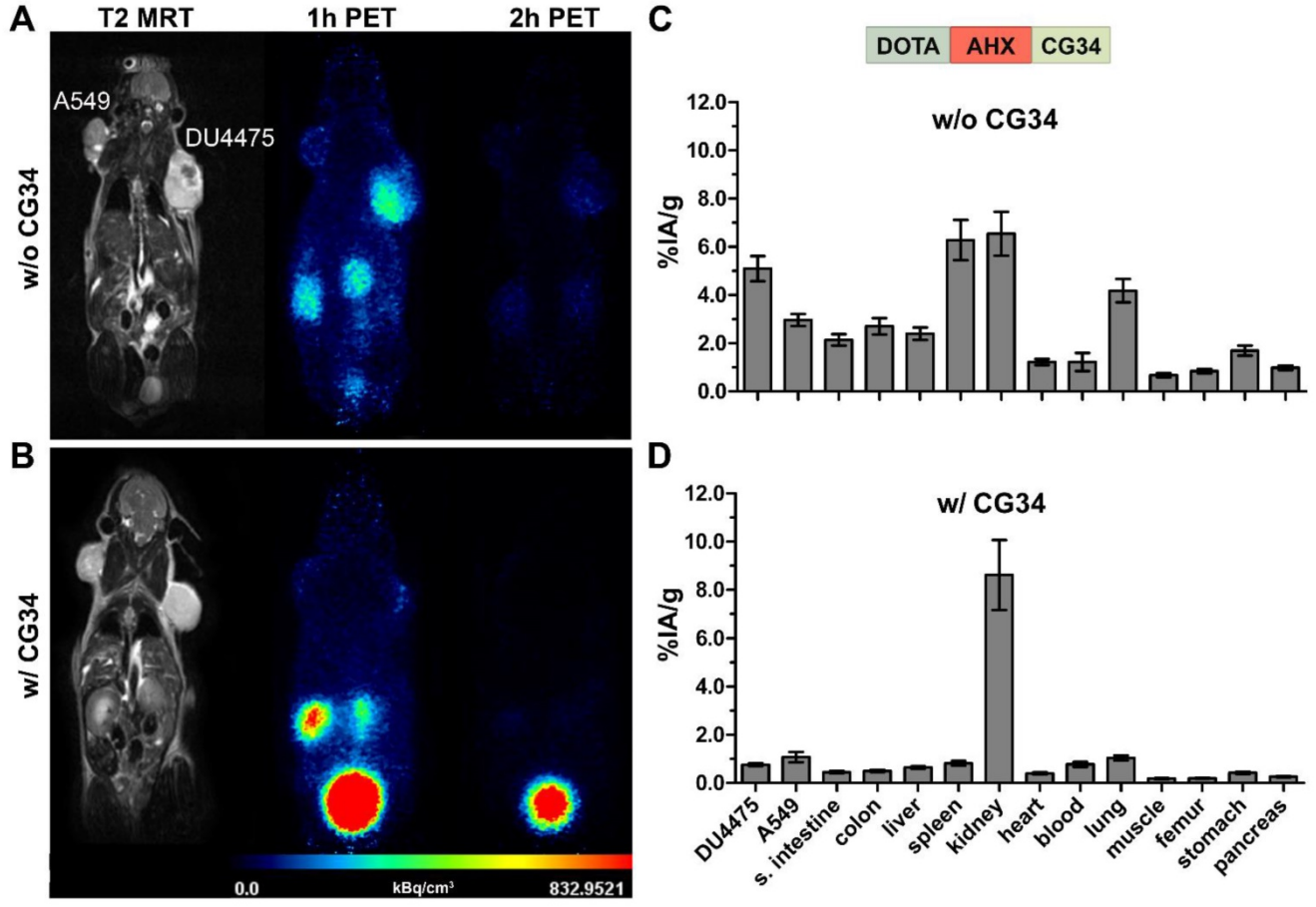

Figure 5: PET/MR imaging and biodistribution study along with a blocking experiment. Representative static PET images were acquired for 30 minutes one and two hours p.i. of ^{68}Ga-labeled DOTA-AHX-CG34 conjugate **(A)** without and **(B)** with coinjected 50-fold excess of unlabeled peptide CG34 (200 nmol) in the same animal. 20 MBq of the tracer were injected intravenously. PET images show a strong DU4475 uptake, which could be completely displaced with excess of non-labeled peptide. Quantitative analysis of tracer biodistribution (10 MBq) one hour p.i. **(C)** without and **(D)** with receptor blocking confirmed the specific tracer uptake in the DU4475 tumor. ($6 \leq n \leq 13$; mean ± SEM)

Table 1: Biodistribution data and tissue radioactivity ratios of ^{68}Ga-labeled chemerin tracers in the DU4475/A549 xenograft model. Data are presented as mean ± SEM (2 ≤ n ≤ 16) % IA/g of tissue or as a ratio. Blocking studies were performed in the presence of 200 nmol of CG34. (n.d. = not determined)

	[^{68}Ga]Ga-DOTA-AHX-CG34			[^{68}Ga]Ga-DOTA-KCap-CG34			[^{68}Ga]Ga-DOTA-ADX-CG34		
organ	1 h	1 h-blocked	2 h	1 h	1 h-blocked	2 h	1 h	1 h-blocked	2 h
DU4475	5.1 ± 0.5	0.8 ± 0.1	4.9 ± 0.8	3.3 ± 0.2	0.6 ± 0.1	2.9 ± 0.5	6.2 ± 0.5	1.8 ± 0.1	4.2 ± 1.0
A549	3.0 ± 0.3	1.1 ± 0.2	1.4 ± 0.1	2.3 ± 0.4	0.6 ± 0.1	n.d.	2.7 ± 0.4	1.6 ± 0.2	n.d.
small intestine	2.1 ± 0.2	0.4 ± 0.0	2.0 ± 0.4	2.3 ± 0.1	0.3 ± 0.1	1.9 ± 0.3	3.8 ± 0.2	1.4 ± 0.2	4.4 ± 2.0
colon	2.7 ± 0.3	0.5 ± 0.0	2.6 ± 0.7	2.4 ± 0.2	0.3 ± 0.0	1.7 ± 0.2	3.2 ± 0.3	1.2 ± 0.1	2.3 ± 0.3
liver	2.4 ± 0.3	0.6 ± 0.0	2.4 ± 0.4	2.2 ± 0.1	0.3 ± 0.0	1.8 ± 0.2	14.2 ± 1.1	10.4 ± 0.9	12.5 ± 1.1
spleen	6.3 ± 0.8	0.8 ± 0.1	5.0 ± 0.5	4.9 ± 0.5	0.5 ± 0.1	4.0 ± 0.6	7.8 ± 0.6	2.3 ± 0.4	5.4 ± 1.0
kidney	6.5 ± 0.9	8.6 ± 1.4	6.6 ± 1.1	5.8 ± 0.9	5.2 ± 0.9	6.5 ± 1.3	10.3 ± 1.7	14.5 ± 3.9	5.5 ± 1.6
heart	1.2 ± 0.1	0.4 ± 0.0	1.1 ± 0.3	1.1 ± 0.1	0.2 ± 0.0	0.8 ± 0.1	2.2 ± 0.2	1.4 ± 0.1	1.2 ± 0.1
blood	1.2 ± 0.4	0.8 ± 0.1	0.4 ± 0.1	0.6 ± 0.1	0.5 ± 0.1	0.2 ± 0.0	2.8 ± 0.7	3.2 ± 0.3	0.8 ± 0.1
lung	4.2 ± 0.5	1.0 ± 0.1	2.8 ± 0.3	1.7 ± 0.1	0.5 ± 0.1	1.2 ± 0.1	7.1 ± 0.7	3.4 ± 0.2	3.9 ± 0.4
muscle	0.7 ± 0.1	0.2 ± 0.0	0.5 ± 0.1	0.6 ± 0.1	0.2 ± 0.1	0.4 ± 0.1	1.1 ± 0.1	0.6 ± 0.1	0.6 ± 0.1
femur	0.8 ± 0.1	0.2 ± 0.0	0.7 ± 0.1	0.6 ± 0.1	0.2 ± 0.1	0.5 ± 0.1	1.3 ± 0.2	0.7 ± 0.1	0.7 ± 0.1
stomach	1.7 ± 0.2	0.4 ± 0.0	1.3 ± 0.1	1.4 ± 0.1	0.3 ± 0.1	1.1 ± 0.2	2.2 ± 0.2	1.1 ± 0.1	1.5 ± 0.2
pancreas	1.0 ± 0.1	0.3 ± 0.0	0.8 ± 0.1	0.9 ± 0.1	0.2 ± 0.0	0.7 ± 0.1	1.7 ± 0.2	0.8 ± 0.1	1.1 ± 0.1
tumor-to-blood	5.9 ± 0.7	1.0 ± 0.1	13.3 ± 3.0	5.6 ± 0.5	1.3 ± 0.3	18.2 ± 3.4	3.0 ± 0.3	0.6 ± 0.1	5.7 ± 1.1
tumor-to-liver	2.3 ± 0.2	1.2 ± 0.0	2.2 ± 0.5	1.6 ± 0.1	1.8 ± 0.3	1.8 ± 0.4	0.4 ± 0.0	0.2 ± 0.0	0.3 ± 0.1
tumor-to-kidney	0.9 ± 0.1	0.1 ± 0.0	0.7 ± 0.1	0.7 ± 0.1	0.1 ± 0.0	0.6 ± 0.1	0.8 ± 0.1	0.2 ± 0.0	0.8 ± 0.2
tumor-to-pancreas	5.6 ± 0.7	2.9 ± 0.2	6.2 ± 1.3	3.7 ± 0.3	3.7 ± 0.5	4.3 ± 0.9	3.9 ± 0.3	2.3 ± 0.2	3.9 ± 0.7
tumor-to-muscle	8.5 ± 1.0	4.4 ± 0.3	11.4 ± 2.4	6.6 ± 0.7	4.3 ± 0.9	7.2 ± 1.2	6.3 ± 0.5	3.3 ± 0.3	7.2 ± 1.2

Lutetium-labeling of chemerin tracers maintained high receptor affinity and target recognition in CMKLR1 tumor model

For further evaluation of their theranostics potential, the probes were labeled with therapeutically relevant metal ions. Thereby, the impact of modified chelation on receptor affinity was assessed. DOTA labeling with native non-radioactive lutetium and yttrium (^{nat}Lu and ^{nat}Y) yielded high-affinity peptide conjugates with IC_{50} values between 0.8 and 2.6 nM (Figure 6A and B) as compared to the gallium-labeled tracers (IC_{50} values between 0.3 and 0.7 nM; Figure 2D). In order to prepare for therapeutic use, ^{177}Lu-labeled tracer DOTA-AHX-CG34 was used for an initial biodistribution study (Figure 6C). The overall tissue activity distribution one hour p.i. was comparable to the ^{68}Ga-labeled tracer (Figure 5C) with 1.4-fold higher uptake in DU4475 (3.3% IA/g) than A549 (2.3% IA/g) and apparent values of spleen (5.8% IA/g), kidneys (4.7% IA/g) and lung (5.6% IA/g). After 24 hours, most of the tissue activity diminished with only low values left for spleen (1.7% IA/g) and kidneys (1.0% IA/g). However, the uptake of target-positive DU4475 tumor was 2.1% IA/g (approx. 64% of the 1 h-value) and with this 5.3-fold higher than the A549 value (0.4% IA/g) 24 hours p.i.

Discussion and Conclusions

The purpose of this study was to evaluate a family of five novel CMKLR1 tracers for their capacity to generate target-specific signals in a breast cancer xenograft mouse model. To the best of our knowledge, this is the first report of CMKLR1 *in vivo* imaging. Although known for its role in inflammation and metabolic regulation for many years, CMKLR1 and its chemokine-like ligand chemerin were only recently recognized as modulators of tumor proliferation and expansion. Other labs have reported overexpression and functional involvement of CMKLR1 in esophageal squamous cell carcinoma, hepatocellular carcinoma, neuroblastoma and gastric cancer [19-22]. Here, we introduce two peptide analogs of chemerin for use in receptor-mediated tumor targeting. These peptide analogs are based on chemerin-9, which has full agonistic activity towards the receptor CMKLR1 and corresponds to the C-terminal nine amino acids of processed chemerin [14]. In a previous study, we have shown the potential to generate stable and potent chemerin-9 analogs by the introduction of D-amino acids via an evolutionary algorithm [24]. The resulting peptide analogs showed improved properties concerning receptor activation, binding affinity and metabolic stability. In this study, we have made use of such analogs as components of chelator conjugates to do PET/MR imaging in a breast cancer xenograft mouse model.

The suitability of the animal model with CMKLR1-positive DU4475 and CMKLR1-negative A549 xenograft tumors was confirmed by immunofluorescence staining and radioligand binding studies. As expression of proteins in cells may change upon transfer from the culture dish monolayer to three-dimensional subcutaneous xenograft in mice, we also investigated CMKLR1 expression in tumor tissue. Thereby, overexpression as well as ligand binding were established for DU4475 tumors while A549 tumors were confirmed as a negative control.

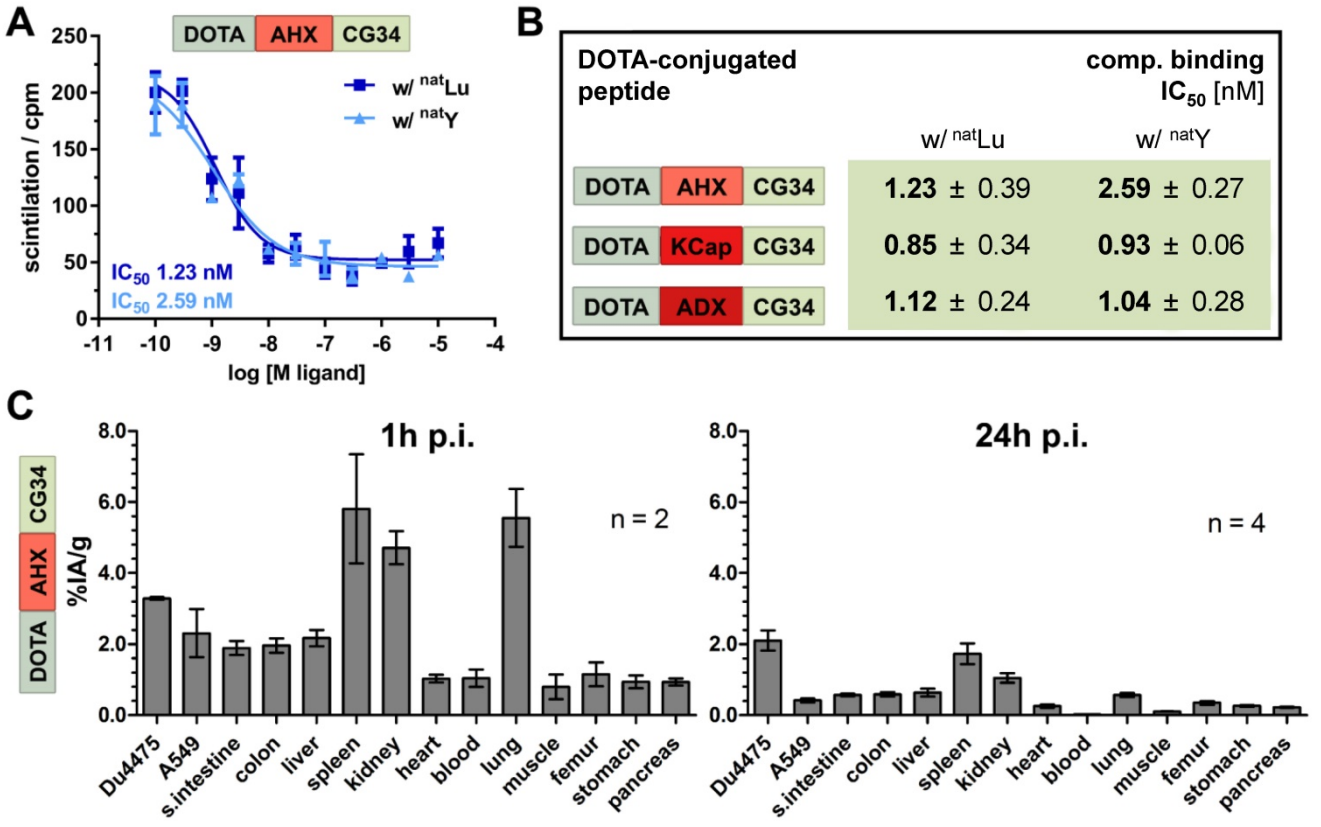

Figure 6: Binding affinity and biodistribution of lutetium- and yttrium-labeled chemerin tracers. (A) Ligand affinity to CMKLR1 was assessed by competitive radioligand binding experiments using ^{125}I-chemerin-9 as radioligand. Displacement binding curves revealed similar IC_{50} values of the ^{nat}Lu-labeled and ^{nat}Y-labeled DOTA-AHX-CG34 conjugate indicating a maintained high affinity around 1 nM. Data are shown as mean ± SEM of two independent experiments. **(B)** Binding assays were performed accordingly for the three CG34 conjugates with AHX, KCap and ADX linker (summarized as IC_{50} values). All IC_{50} values were obtained from two independent experiments and are indicated as means ± SD. **(C)** For quantitative analysis of tracer biodistribution, approx. 1 MBq of the ^{177}Lu-labeled tracer DOTA-AHX-CG34 was injected intravenously and tissue was analyzed *ex vivo* one or 24 hours p.i. Values for tracer uptake are indicated as percent injected activity per gram tissue (% IA/g). Biodistribution after one hour shows an apparent uptake in DU4475 (3.3% IA/g), and less in A549 tumors (2.3% IA/g). Furthermore, the tracer accumulated in the kidneys, spleen and lung and led to a biodistribution comparable to the ^{68}Ga-labeled tracer. After 24 hours, the highest uptake was detectable in DU4475 tumors with approx. 2.1% IA/g ($2 \leq n \leq 4$; mean ± SEM).

In the design of our tracers, we followed the hypothesis that tumor uptake and biodistribution may depend on a balance of hydrophobic and hydrophilic properties within the molecule. Therefore, we chose not only to make use of a more hydrophilic and a more hydrophobic CMKLR1 peptide ligand analog, but also to take advantage of different linkers to introduce a varying degree of hydrophobicity into the conjugates. As the chelator DOTA with its four carboxylic groups confers rather strong hydrophilic features, we chose to compensate this with mainly hydrophobic linker moieties: 6-aminohexanoic acid (AHX), N-ε-capryloyl-lysine (KCap) and 10-aminodecanoic acid (ADX). Only one linker displayed rather hydrophilic properties: the polyethylene glycol (PEG)-like 4,7,10-trioxatridecan-succinamic acid (TTDS) (Figure 2A). Unexpectedly, the $LogD_{7.4}$ values of AHX and TTDS compounds were rather similar (-0.96 and -1.01, respectively). The ADX and KCap conjugates also showed comparable hydrophobicity ($LogD_{7.4}$ approximately 1.3), while the only CG36 conjugate was considerably more hydrophobic ($LogD_{7.4}$ 2.27). This set of five DOTA peptide conjugates was tested *in vitro* prior to the animal study. Of note, all these tracers proved to be of high affinity and functional activity, with IC_{50} and EC_{50} values being below 2 nM (Figure 2D). Affinity also did not change significantly upon complexation of DOTA with natural non-radioactive gallium (^{nat}Ga), and if so, IC_{50} values even improved. This was in many ways unexpected as we and others had often experienced an impairment of the binding and activating capacity of ligands upon conjugation with a linker and a reporter such as a chelator or dye molecule [25-28]. Likewise, the affinity of such a conjugate may be affected by the coordination of a radiometal ion [29]. The structural requirements of chemerin analogs binding to CMKLR1 obviously allow for a broad variety of additions to the N-terminus of the nonameric peptide. Even though the two most potent conjugates were the ones with the shortest linkers (AHX and ADX), differences were small and a significant systematic influence of linker hydrophobicity or length on affinity or activity was not observed.

The initial PET studies using all five tracers revealed a clear difference regarding tumor uptake and biodistribution: the most hydrophilic conjugate ([^{68}Ga]Ga-DOTA-TTDS-CG34) and the most hydrophobic conjugate ([^{68}Ga]Ga-DOTA-AHX-CG36) both showed lower tumor and higher kidney uptake than the three conjugates with balanced hydrophilicity in the molecule (Figure 3). This was also confirmed by results from biodistribution experiments: for both tracers, there was no clear difference in uptake between target-positive and target-negative tumor (Figure S1 and Table S2). These results may indicate the validity of our hypothesis that sufficient and specific tumor uptake may be achieved best using a conjugate with moderate, balanced hydrophilicity. Both highly hydrophobic and strongly hydrophilic tracers may primarily yield unspecific uptake in kidney and liver. Liver uptake is notable for the tracer [^{68}Ga]Ga-DOTA-ADX-CG34 with 14.2% IA/g at one hour, 12.5% IA/g at two hours. In addition, [^{68}Ga]Ga-DOTA-AHX-CG36 shows 6.4% and 4.9% liver uptake (IA/g), respectively. The other three probes do not accumulate in the liver more than 2.6% IA/g at any time. High liver uptake may yield a significant radiation dose delivered to the healthy organ, limiting its potential therapeutic utility. Moreover, imaging of metastatic lesions in the liver might be constricted.

By peptide optimization and conjugation, we were able to obtain a family of five high-potency, high-affinity molecular probes for further *in vivo* application as radiotracers. In addition to PET/MRI scans one and two hours post-injection, *ex vivo* biodistribution studies were performed to assess quantitative values for tissue uptake. Utilizing a breast-cancer xenograft mouse model, PET/MRI and concomitant biodistribution studies revealed the specificity of our chemerin-based radiotracers by distinct PET signals and uptake values of CMKLR1-positive DU4475 tumors compared to no PET visibility and low tumor radioactivity values of target-negative A549 tumors. The moderate tracer uptake seen in the latter is probably due to unspecific mechanisms such as non-selective transporters, hydrophobic interaction or blood pool activity. Kidney uptake often limits therapeutic use of tracers. For the three best tracers described in this study, renal uptake was between 5.8 to 10.3% IA/g, resulting in favorable tumor-to-kidney ratios of 0.7 to 0.9 at one hour post injection.

Further evidence for the specificity of the tracer was obtained in a blocking experiment with an excess of non-labeled peptide (Figure 5). As obvious from both PET/MR images as well as biodistribution data, this excess strongly reduced uptake of the tracer [^{68}Ga]Ga-DOTA-AHX-CG34 in CMKLR1-positive DU4475 tumors, indicating displacement of the radioligand from its receptor. The lower uptake observed in other organs probably also corresponds to tracer displacement from chemerin receptors known to be expressed there (e.g. lung, spleen) [11, 30]. The dynamic PET scan of [^{68}Ga]Ga-DOTA-AHX-CG34 showed faster background/off-target clearance as well as fast and stable accumulation at tumor sites. Higher hydrophobicity of KCap and ADX may have contributed to delayed and prolonged kidney uptake, possibly due to plasma protein binding or metabolization in the liver (Figure S2).

While a tumor uptake of 3 to 6% represents a promising targeting result for these first CMKLR1 tracers, several options for an improvement remain. One current limitation, especially for an application in peptide receptor radionuclide therapy (PRRT), is the fast elimination of the signal from the target-positive tumor. According to biodistribution data, the signal decrease between one hour and two hours in DU4475 tumors was about 5 to 30%. With the tracer [^{177}Lu]Lu-DOTA-AHX-CG34, a 1.4-fold higher uptake in DU4475 (3.3% IA/g) than A549 (2.3% IA/g) was observed. The decrease from one to 24 hours p.i. here was even higher (approximately 36%) than for the corresponding ^{68}Ga compound. Before a therapeutic application can be considered, uptake and persistence in the tumor should be improved, i.e. by modulating the molar activity of the tracer. Although the underlying peptide analogs have been selected for their improved stability in *in vitro* protease degradation assays, a degradation due to proteolytic activity in circulation and target tissue may play a role. Similarly, fast excretion via the renal pathway, as well as hepatic degradation (e.g. [^{68}Ga]Ga-DOTA-ADX-CG34) may create unfavorable distribution kinetics. The precise causes for this rapid decrease in tumor signal will have to be determined in subsequent studies. Biochemical isolation and analysis of tracer metabolites from the animal's circulation may provide a means of clarifying the underlying mechanism.

Abbreviations

% IA/g: percent injected activity per gram tissue; ^{177}Lu: lutetium-177; [^{18}F]-FDG: [^{18}F]fluoro-deoxy-glucose; ^{68}Ga: gallium-68; ADX: 10-aminodecanoic acid; AHX: 6-aminohexanoic acid; BERIC: Berlin Experimental Radionuclide Imaging Center; BSA: bovine serum albumin; CG34: chemerin analog with amino acid sequence Y-Cha-Hyp-G-Cit-F-a-Tic-S; CG36: chemerin analog with amino acid sequence Y-Cha-P-G-M-Y-A-F-f; chemerin-9: nonapeptide Y-F-P-G-Q-F-A-F-S; CMKLR1: chemokine-like

receptor 1; DMSO: dimethyl sulfoxide; DOTA: 1,4,7,10-tetraazacyclododecane-1,4,7,10-tetraacetic acid; DTPA: diethylenetriaminepentaacetic acid; EC_{50}: half maximal effective concentration; ECM: extracellular matrix; EGFR: epithelial growth factor receptor; EGTA: ethylene glycol-bis(β-aminoethyl ether)-N,N,N′,N′-tetraacetic acid; ESCC: esophageal squamous cell carcinoma; G418: geneticin; GMP: good manufacturing practice; GPCR: G protein-coupled receptor; HEPES: 4-(2-hydroxyethyl)-1-piperazineethanesulfonic acid; HPLC: high-performance liquid chromatography; IC_{50}: half maximal inhibitory concentration; KCap: N-ε-capryloyl-lysine; MRI: magnetic resonance imaging; n.d.: not determined; NET: neuroendocrine tumor; NMRI: Naval Medical Research Institute; PBS: phosphate-buffered saline; PEG: polyethylene glycol; PET: positron emission tomography; PRRT: peptide receptor radionuclide therapy; PSMA: prostate-specific membrane antigen; RPMI1640: Roswell Park Memorial Institute medium 1640; SD: standard deviation; SEM: standard error of the mean; SSA: somatostatin analog; SSTR: somatostatin receptor; T2 FSE 2D: high-resolution T2-weighted 2D fast spin echo sequence; TBS: Tris-buffered saline; TE: echo time; TFA: trifluoroacetic acid; TR: repetition time; TTDS: 4,7,10-trioxatridecan-succinamic acid; VOI: volume of interest.

Supplementary Material

Supplementary figures and tables.
http://www.thno.org/v09p6719s1.pdf

Acknowledgements

This work was supported by a grant from the German Ministry of Education and Research (BMBF grant IPT614A to CG). Samantha Exner was the recipient of a fellowship by Sonnenfeld-Stiftung. We acknowledge support from the German Research Foundation (DFG) and the Open Access Publication Funds of Charité – Universitätsmedizin Berlin.

Author Contributions

Concept and experimental design: S.Er., C.G., W.B. Development of methodology: S.Er., C.G. Acquisition of data: S.Er., L.N., E.J.K., J.D.C.G., S.P., A.W., J.L.v.H., S.R., S.Ex., S.B. Analysis and interpretation of data: S.Er., C.G. Writing, review, and/or revision of the manuscript: S.Er., E.J.K., N.B., W.B., C.G. and all other authors. Study supervision: W.B., C.G.

Competing Interests

The authors have declared that no competing interest exists.

References

1. Sai KKS, Zachar Z, Bingham PM, Mintz A. Metabolic PET Imaging in Oncology. AJR Am J Roentgenol. 2017; 209: 270-6.
2. Backer MV, Backer JM. Imaging key biomarkers of tumor angiogenesis. Theranostics. 2012; 2: 502-15.
3. Ke X, Shen L. Molecular targeted therapy of cancer: The progress and future prospect. Frontiers in Laboratory Medicine. 2017; 1: 69-75.
4. Padma VV. An overview of targeted cancer therapy. Biomedicine (Taipei). 2015; 5: 19.
5. Nieto Gutierrez A, McDonald PH. GPCRs: Emerging anti-cancer drug targets. Cell Signal. 2018; 41: 65-74.
6. Insel PA, Sriram K, Wiley SZ, Wilderman A, Katakia T, McCann T, et al. GPCRomics: GPCR Expression in Cancer Cells and Tumors Identifies New, Potential Biomarkers and Therapeutic Targets. Front Pharmacol. 2018; 9: 431.
7. Chames P, Van Regenmortel M, Weiss E, Baty D. Therapeutic antibodies: successes, limitations and hopes for the future. Br J Pharmacol. 2009; 157: 220-33.
8. Fani M, Maecke HR, Okarvi SM. Radiolabeled peptides: valuable tools for the detection and treatment of cancer. Theranostics. 2012; 2: 481-501.
9. Kamath AV. Translational pharmacokinetics and pharmacodynamics of monoclonal antibodies. Drug Discov Today Technol. 2016; 21-22: 75-83.
10. Zhao N, Qin Y, Liu H, Cheng Z. Tumor-Targeting Peptides: Ligands for Molecular Imaging and Therapy. Anticancer Agents Med Chem. 2018; 18: 74-86.
11. Yoshimura T, Oppenheim JJ. Chemokine-like receptor 1 (CMKLR1) and chemokine (C-C motif) receptor-like 2 (CCRL2); two multifunctional receptors with unusual properties. Exp Cell Res. 2011; 317: 674-84.
12. Ernst MC, Haidl ID, Zuniga LA, Dranse HJ, Rourke JL, Zabel BA, et al. Disruption of the chemokine-like receptor-1 (CMKLR1) gene is associated with reduced adiposity and glucose intolerance. Endocrinology. 2012; 153: 672-82.
13. Bondue B, Wittamer V, Parmentier M. Chemerin and its receptors in leukocyte trafficking, inflammation and metabolism. Cytokine Growth Factor Rev. 2011; 22: 331-8.
14. Wittamer V, Gregoire F, Robberecht P, Vassart G, Communi D, Parmentier M. The C-terminal nonapeptide of mature chemerin activates the chemerin receptor with low nanomolar potency. J Biol Chem. 2004; 279: 9956-62.
15. Mattern A, Zellmann T, Beck-Sickinger AG. Processing, signaling, and physiological function of chemerin. IUBMB Life. 2014; 66: 19-26.
16. Ferland DJ, Watts SW. Chemerin: A comprehensive review elucidating the need for cardiovascular research. Pharmacol Res. 2015; 99: 351-61.
17. Pachynski RK, Zabel BA, Kohrt HE, Tejeda NM, Monnier J, Swanson CD, et al. The chemoattractant chemerin suppresses melanoma by recruiting natural killer cell antitumor defenses. J Exp Med. 2012; 209: 1427-35.
18. Parolini S, Santoro A, Marcenaro E, Luini W, Massardi L, Facchetti F, et al. The role of chemerin in the colocalization of NK and dendritic cell subsets into inflamed tissues. Blood. 2007; 109: 3625-32.
19. Kumar JD, Kandola S, Tiszlavicz L, Reisz Z, Dockray GJ, Varro A. The role of chemerin and ChemR23 in stimulating the invasion of squamous oesophageal cancer cells. Br J Cancer. 2016; 114: 1152-9.
20. Tummler C, Snapkov I, Wickstrom M, Moens U, Ljungblad L, Maria Elfman LH, et al. Inhibition of chemerin/CMKLR1 axis in neuroblastoma cells reduces clonogenicity and cell viability *in vitro* and impairs tumor growth *in vivo*. Oncotarget. 2017; 8: 95135-51.
21. Li JJ, Yin HK, Guan DX, Zhao JS, Feng YX, Deng YZ, et al. Chemerin suppresses hepatocellular carcinoma metastasis through CMKLR1-PTEN-Akt axis. Br J Cancer. 2018; 118: 1337-48.
22. Kumar JD, Aolymat I, Tiszlavicz L, Reisz Z, Garalla HM, Beynon R, et al. Chemerin acts via CMKLR1 and GPR1 to stimulate migration and invasion of gastric cancer cells: putative role of decreased TIMP-1 and TIMP-2. Oncotarget. 2019; 10: 98-112.
23. Greenwood FC, Hunter WM, Glover JS. The Preparation of I-131-Labelled Human Growth Hormone of High Specific Radioactivity. Biochem J. 1963; 89: 114-23.
24. Bandholtz S, Wichard J, Kuhne R, Grotzinger C. Molecular evolution of a peptide GPCR ligand driven by artificial neural networks. PLoS One. 2012; 7: e36948.
25. Fani M, Del Pozzo L, Abiraj K, Mansi R, Tamma ML, Cescato R, et al. PET of somatostatin receptor-positive tumors using 64Cu- and 68Ga-somatostatin antagonists: the chelate makes the difference. J Nucl Med. 2011; 52: 1110-8.
26. Zhang X, Wang B, Zhao N, Tian Z, Dai Y, Nie Y, et al. Improved Tumor Targeting and Longer Retention Time of NIR Fluorescent Probes Using Bioorthogonal Chemistry. Theranostics. 2017; 7: 3794-802.

27. Chen Y, Pullambhatla M, Banerjee SR, Byun Y, Stathis M, Rojas C, et al. Synthesis and biological evaluation of low molecular weight fluorescent imaging agents for the prostate-specific membrane antigen. Bioconjug Chem. 2012; 23: 2377-85.
28. Mankoff DA, Link JM, Linden HM, Sundararajan L, Krohn KA. Tumor receptor imaging. J Nucl Med. 2008; 49 Suppl 2: 149S-63S.
29. Ginj M, Maecke HR. Radiometallo-labeled peptides in tumor diagnosis and therapy. Met Ions Biol Syst. 2004; 42: 109-42.
30. Kennedy AJ, Davenport AP. International Union of Basic and Clinical Pharmacology CIII: Chemerin Receptors CMKLR1 (Chemerin1) and GPR1 (Chemerin2) Nomenclature, Pharmacology, and Function. Pharmacol Rev. 2018; 70: 174-96.